Article

Journal of Vibration and Control
2017, Vol. 23(4) 615–631

DOI: 10.1177/1077546315581944
journals.sagepub.com/home/jvc
SAGE

On a hybrid use of structural vibration signatures for damage identification: a virtual vibration deflection (VVD) method

Hao Xu[1,2], Zhongqing Su[1,2], Li Cheng[1,2] and Jean-Louis Guyader[3]

Abstract

A damage identification method named virtual vibration deflection (VVD) was developed, the principle of which was formulated based on the "weak" modality of the pseudo-excitation (PE) approach previously established. In essence, VVD is based on locating structural damage within a series of "sub-regions" divided from the entire structure under inspection, and each sub-region was considered as a "virtual" structure undergoing independent vibration. The corresponding vibration deflection of the "virtual" structure was then used to derive the damage index of VVD. Besides various advantages inheriting from the PE approach, for example, capability of detecting damage without baseline signals and pre-developed benchmark structures, VVD exhibits improved detection accuracy and particularly enhanced noise immunity compared with the PE approach, attributed to a hybrid use of multi-types of vibration signatures (MTVS). As a proof-of-concept investigation, a beam model was used in a numerical study to examine the philosophy of VVD. And the influences from different factors (i.e., level of measurement noise and measurement density) on the detection accuracy of VVD were discussed based on the numerical model. An experiment was carried out subsequently to identify the locations of multiple defects contained in an aluminum beam-like structure. Identification results constructed by the PE approach, VVD using single-type of vibration signatures, and VVD using MTVS, were presented, respectively, for the purpose of comparison.

Keywords

Damage identification, noise immunity, vibration signature, virtual vibration, weighted integration

1. Introduction

Damage identification relying on examination of changes in structural vibration signatures has attracted intensive studies for decades (Farrar et al., 2001; Fan and Qiao, 2011; Liu et al., 2011; He et al., 2014). Until now, variations in a number of vibration signatures, such as eigen-frequencies (Lee and Chung, 2000; Wang et al., 2001; Guo and Li, 2011; Pau et al., 2010), mode shapes (Kim et al., 2003; Cao et al., 2013a), curvature mode shapes (Pandey et al., 1991; Montalvao et al., 2006; Qiao et al., 2007; Tomaszewska, 2010; Ciambella and Vestroni, 2015), flexibility matrix (Aoki and Byon, 2001; Yan and Golinval, 2005) and damping properties (Kawiecki, 2001), were proven to be correlated with the existence, location or even severity of structural damage. However, the effectiveness of most existing vibration-based methods suffers from crucial limitations hampering their wide applications in engineering practices. For example, excessive reliance on baseline signals captured from pre-constructed benchmark structures. Under usual circumstances, it was accepted that it was a challenging task to build the benchmark structures in an

[1]The Hong Kong Polytechnic University Shenzhen Research Institute, Shenzhen, China
[2]Department of Mechanical Engineering, The Hong Kong Polytechnic University, Hong Kong
[3]Laboratoire Vibrations Acoustique, Institut National des Sciences Appliquées (INSA) de Lyon, France

Received: 2 December 2014; accepted: 19 March 2015

Corresponding author:
Zhongqing Su, Department of Mechanical Engineering, The Hong Kong Polytechnic University, Hong Kong SAR.
Email: MMSU@polyu.edu.hk

accurate manner, through either a numerical or experimental means. This can be attributed to the complexity of material and geometric features of a real structure, in particular when vast environmental uncertainties were involved (Stubbs and Kim, 1996).

Aimed at addressing the above issues, the pseudo-excitation (PE) approach was developed based on the examination of local dynamic equilibrium of different structural components (Xu et al., 2011, 2013a,b). With an explicit physical implication (i.e., associated with the condition of dynamic equilibrium), the damage index of the PE is able to reveal damage locations and even sizes in the absence of baseline signals and benchmark structures, as long as several basic parameters relating to structural material and geometry (e.g., Young's modulus) are known. Typified by local inspection, the application of the PE is independent of any prior knowledge of structural boundary conditions, and can be effectively performed using vibration signals generated under structural operational state. Thus the reliance on well controlled external excitation sources, which is of necessity for a variety of damage identification methods, particularly those utilizing characteristics of guided waves (Giurgiutiu, 2005; Wang et al., 2006; Zhao et al., 2007; Su et al., 2007; 2009; Ihn and Chang, 2008; Chen et al., 2010; Zhou et al., 2011; Sohn et al., 2014), can be prevented.

Involving high-order derivatives of vibration displacements, the damage index of the PE approach showed high sensitivity to measurement noise that was unavoidable under experimental conditions. To reduce the noise influence, the ''weak'' formulation of the PE was developed by introducing weighted integration to the original differential equation. Depending on proper selections of integration interval, and particularly the form of weighting function, measurement noise was largely suppressed within the integration interval. More importantly, the ''weak'' formulation was able to achieve a variety of advantages besides noise reduction, for example, the flexibility of opting for various types of mechanical quantities to be measured at those positions which are arbitrarily selected. These advantages enable developments of new strategies of damage detection with enriched options of experimental configurations, capable of reaching improved detection accuracy and precision.

Virtual vibration deflection (VVD) was established based on the ''weak'' formulation of the PE approach, with unique theoretical expressions and experimental configurations. The essence of VVD is based on identifying damage within a series of sub-regions, equivalent as the integration intervals of the ''weak'' formulation, divided from the entire structure under inspection. Each sub-region is deemed as a ''virtual'' structure undergoing independent vibration. Interestingly, the vibration deflection of the ''virtual'' structure, calculated according to the classic mode superposition method, can be used as the weighting function included in the ''weak'' formulation. Consequently, the damage index of VVD can be constructed using the calculated weighing function. Different from the PE which is established based on single-type of vibration signatures (STVS) (only vibration displacements were measured and processed), VVD can be constructed relying on the flexible selection of multi-types of vibration signatures (MTVS) (for example, the combination of vibration displacements and curvatures).

Originated from the PE approach, VVD naturally inherits the various advantages of the PE (e.g., independences of baseline signals and benchmark structures) as mentioned above.Moreover, VVD is capable of achieving improved detection accuracy and noise immunity compared with the PE approach, attributed to a hybrid use of MTVS. In engineering practices (particularly in civil engineering), it is common that MTVS are captured along inspected structures using different types of sensors (Zhang et al., 2011), so as to achieve optimal detection results. In most cases, however, different types of vibration signatures can only be used separately by distinct damage identification methods, causing less efficient use of the database comprising of a great number of measurands. From this respect, VVD increases the efficiency of the utilization of the existing database, providing the additional benefit of improving detection accuracy.

As a proof-of-concept investigation, a finite element (FE) model of a cantilever beam containing a small damaged zone was used to examine the philosophy of VVD. And the influences from different factors (i.e., level of measurement noise and measurement density) on the detection accuracy of VVD were discussed based on the numerical model. An experiment was carried out subsequently, to identify the locations of multiple defects in an aluminum beam-like structure. Identification results constructed using the PE approach, VVD using MTVS (i.e., densely measured vibration displacements and sparsely measured dynamic strains), and VVD using STVS, were presented, respectively, for the purpose of comparison.

2. The pseudo-excitation approach and its "Weak" formulation

Damage indices of the PE approach were established based on equations of motion for various types of structural components, e.g., beam, plate or shell component. Using a homogeneous isotropic Euler-Bernoulli beam component as an example, the damage index under steady vibration state can be

expressed as

$$\mathrm{DI}(x) = EI\frac{\mathrm{d}^4 w(x)}{\mathrm{d}x^4} - \rho S\omega^2 w(x) \tag{1a}$$

where $w(x)$ is the vibration displacement at location x; ω is the angular vibration frequency of the beam; E, ρ, I and S are the modulus of elasticity, density, cross-sectional moment of inertia and area of the beam under pristine status, respectively. In classic beam vibration theory, $\mathrm{DI}(x)$ represents the distribution of external excitation applied on the axis of an undamaged beam, and $\mathrm{DI}(x) = 0$ signifies the absence of external excitation (in ideal cases, $\mathrm{DI}(x)$ remains zero for a beam subject to point excitations or excitations located at structural boundaries). It was found in previous study (Xu et al., 2011), however, the $\mathrm{DI}(x)$ showed variations from zero at damaged zones contained in a beam, whereas remained zero at intact regions of the beam. More importantly, prominent oscillations of $\mathrm{DI}(x)$ were discovered at the boundaries of damaged zones, which can be well utilized to precisely indicate the locations and sizes of damage. Because of the similarity between structural damage and external excitation in causing variations of $\mathrm{DI}(x)$, the signal of $\mathrm{DI}(x)$ in equation (1a), used for damage identification, was defined as PE.

In practical implementation, $w(x)$ should be discretely measured in experiments. Thus the above $\mathrm{DI}(x)$, at a target point i, can be constructed using a finite difference method in a discrete form (if four neighboring measurement points from point $i-2$ to $i+2$ are involved), as

$$\mathrm{DI}_i = \frac{EI}{\Delta^4}(w_{i-2} - 4w_{i-1} + 6w_i - 4w_{i+1} + w_{i+2}) - \rho S\omega^2 w_i \tag{1b}$$

where Δ is the distance between adjacent measurement points, w_i the flexural displacement measured at point i. Similarly, a two-dimensional damage index can be derived based on plate vibration theory, as

$$\mathrm{DI}(x,y) = D\nabla^4 w(x,y) - \rho h\omega^2 w(x,y) \tag{1c}$$

where D, being $Eh^3/12(1-\nu^2)$, signifies the bending stiffness of the plate component; $w(x,y)$ is the vibration displacement; h and ν are the thickness and the Poisson's ratio, respectively. According to a two-dimensional finite difference method, $\mathrm{DI}(x,y)$ in equation (1c) can be discretely constructed (Xu et al., 2013a).

Although with the potential of precise indication of structural damage, the PE approach exhibits great sensitivity to the interference from measurement noise that is unavoidable in a practical application, due to the high-order derivatives of vibration displacements involved in its damage index, as shown in equation (1a). Aimed at noise reduction, the "weak" formulation of the PE was developed by introducing weighted integration to the original formulation characterized by the differential equation. The general form of the "weak" formulation, still using a beam component for instance, can be written as

$$\overline{\mathrm{DI}} = \int_{x_c-\tau/2}^{x_c+\tau/2} [\mathrm{DI}(x)\cdot\eta(x-x_c)]\mathrm{d}x \tag{2}$$

where $\overline{\mathrm{DI}}$ is the re-defined damage index subject to an integration interval of $[x_c-\tau/2, x_c+\tau/2]$ with x_c and τ as its center position and length, respectively. The integration interval is denoted by Ξ in what follows. $\eta(x)$ is a weighting function selected with arbitrary form. When applying the "weak" formulation, the positions and sizes of Ξ and $\eta(x)$ can be adjusted by regulating x_c and τ, offering a "scanning window" to examine the entire beam component. And any variation of $\overline{\mathrm{DI}}$ from zero indicates the existence of damage within Ξ. Depending on proper selections of Ξ and $\eta(x)$, the measurement noise can be considerably averaged and suppressed within Ξ, with more prominent damage-related features highlighted. The significant de-noising effect of the "weak" formulation of the PE by selecting $\eta(x)$ as a classic Gaussian function was detailed in a previous study (Xu et al., 2015). And it was concluded that the principle of noise reduction using equation (2) is similar with that of some existing signal processing techniques such as wavelet transform (Cao et al., 2013b; Xu et al., 2013c).

Specifically, equation (2) can be expanded by substituting equation (1a) into (2), as

$$\overline{\mathrm{DI}}_4 = \int_\Xi \left[EI\frac{\mathrm{d}^4 w(x)}{\mathrm{d}x^4} - \rho S\omega^2 w(x)\right]\eta(x-x_c)\mathrm{d}x \tag{3a}$$

The subscript k in $\overline{\mathrm{DI}}_k$ signifies the highest order of the derivative of $w(x)$ involved in the integration, and $k=4$ in equation (3a). Equation (3a) is defined as the fourth-order "expanded form" of the "weak" formulation. To take further steps, another four expanded forms, from third- to zero-order, can be obtained based on equation (3a) using partial integration, and the zero-order expanded form is expressed as

$$\overline{\mathrm{DI}}_0 = EI\left[\frac{\mathrm{d}^3 w(x)}{\mathrm{d}x^3}\cdot\eta(x-x_c) - \frac{\mathrm{d}^2 w(x)}{\mathrm{d}x^2}\cdot\frac{\mathrm{d}\eta(x-x_c)}{\mathrm{d}x} + \frac{\mathrm{d}w(x)}{\mathrm{d}x}\cdot\frac{\mathrm{d}^2\eta(x-x_c)}{\mathrm{d}x^2} - w(x)\cdot\frac{\mathrm{d}^3\eta(x-x_c)}{\mathrm{d}x^3}\right]_{x_c-\tau/2}^{x_c+\tau/2}$$

$$-\int_{\Xi}\left[EI\frac{\mathrm{d}^4\eta(x-x_c)}{\mathrm{d}x^4}-\rho S\omega^2\cdot\eta(x-x_c)\right]w(x)\mathrm{d}x \quad (3b)$$

Mathematically, equations (3a) and (3b) are identical. Compared with equation (3a), however, equation (3b) offers the possibility to develop new identification strategies for damage with increased flexibilities in parameter selection and experimental configuration, enabling the utilization of MTVS. For example, $\mathrm{d}w(x)/\mathrm{d}x$ in equation (3b) can be obtained by measuring the rotation angle of structural vibration (Abdo and Hori, 2002). And $\mathrm{d}^2w(x)/\mathrm{d}x^2$, defined as $\kappa(x)$ in what follows, is well-known as the curvature of vibration displacement, and can be obtained by measuring dynamic strains. The relationship between $\kappa(x)$ and strain along beam component can be expressed as

$$\varepsilon(x)=\frac{h}{2}\cdot\kappa(x) \quad (4)$$

where $\varepsilon(x)$ is strain, and h is the thickness of the beam component. Besides the involvement of MTVS, the measurement positions of the MTVS can be freely arranged along inspected structure, by adjusting the position and size of Ξ in equation (3b). It is anticipated that by relying on reasonable selections of measurands and measurement positions, equation (3b) is able to attain satisfactory detection accuracy and precision.

3. Virtual vibration deflection

Virtual vibration deflection is then established based on equation (3b). Assuming that a certain form of $\eta(x)$ in equation (3b) exists, satisfying

$$\int_{\Xi}\left[EI\frac{\mathrm{d}^4\eta(x-x_c)}{\mathrm{d}x^4}-\rho S\omega^2\cdot\eta(x-x_c)\right]w(x)\mathrm{d}x=0 \quad (5a)$$

then equation (3b) can be simplified by containing those terms at the boundaries of Ξ only. If further simplification can be made, for example, with the following conditions satisfied:

$$\eta(\tau/2)=0,\quad \eta(-\tau/2)=0,\frac{\mathrm{d}^2\eta(\tau/2)}{\mathrm{d}x^2}=0,\quad \frac{\mathrm{d}^2\eta(-\tau/2)}{\mathrm{d}x^2}=0 \quad (5b)$$

then two more terms in equation (3b) can be eliminated, giving rise to a simple expression of the damage index of VVD, as

$$\begin{aligned}\overline{\mathrm{DI}}_{-VVD}=-EI\Bigg[&\kappa(x_c+\tau/2)\cdot\frac{\mathrm{d}\eta(\tau/2)}{\mathrm{d}x}\\&-\kappa(x_c-\tau/2)\cdot\frac{\mathrm{d}\eta(-\tau/2)}{\mathrm{d}x}\Bigg]\\&-EI\Bigg[w(x_c+\tau/2)\cdot\frac{\mathrm{d}^3\eta(\tau/2)}{\mathrm{d}x^3}\\&-w(x_c-\tau/2)\cdot\frac{\mathrm{d}^3\eta(-\tau/2)}{\mathrm{d}x^3}\Bigg]\end{aligned} \quad (5c)$$

In the above equation, $\kappa(x_c-\tau/2)$, $\kappa(x_c+\tau/2)$, $w(x_c-\tau/2)$ and $w(x_c+\tau/2)$ can be obtained by measuring dynamic strains and vibration displacements, respectively, and $\mathrm{d}\eta(-\tau/2)/\mathrm{d}x$, $\mathrm{d}\eta(\tau/2)/\mathrm{d}x$, $\mathrm{d}^3\eta(-\tau/2)/\mathrm{d}x^3$ and $\mathrm{d}^3\eta(\tau/2)/\mathrm{d}x^3$ can be calculated based on $\eta(x)$. Therefore, the key step of establishing VVD resides on the construction of $\eta(x)$ according to equations (5a) and (5b), to be detailed as follows.

In equation (5a), assuming

$$q(x)=EI\frac{\mathrm{d}^4\eta(x-x_c)}{\mathrm{d}x^4}-\rho S\omega^2\cdot\eta(x-x_c),\quad x\in\Xi \quad (6a)$$

then equation (5a) becomes

$$\int_{\Xi}q(x)w(x)\mathrm{d}x=0 \quad (6b)$$

To calculate $q(x)$, first make it represented by the summation of a trial function, $\widetilde{q}(x)$, and a constant, c, as

$$q(x)=\widetilde{q}(x)+c,\quad x\in\Xi \quad (6c)$$

Since $\widetilde{q}(x)$ can be selected with an explicit form, and the distribution of $w(x)$ is also fixed from experiment, c can be computed according to equation (6b) and (6c), as

$$c=\frac{\int_{\Xi}\widetilde{q}(x)w(x)\mathrm{d}x}{\int_{\Xi}w(x)\mathrm{d}x} \quad (6d)$$

as long as $\int_{\Xi}w(x)\mathrm{d}x\neq 0$. And then $q(x)$ can be explicitly expressed using equation (6c).

With a calculated $q(x)$, equations (5a) and (5b) can be rewritten as

$$EI\frac{\mathrm{d}^4\eta(x-x_c)}{\mathrm{d}x^4}-\rho S\omega^2\cdot\eta(x-x_c)=q(x),\quad x\in\Xi \quad (7a)$$

$$\eta(\tau/2)=0,\quad \eta(-\tau/2)=0,\frac{\mathrm{d}^2\eta(\tau/2)}{\mathrm{d}x^2}=0,\quad \frac{\mathrm{d}^2\eta(-\tau/2)}{\mathrm{d}x^2}=0 \quad (7b)$$

Interestingly, equation (7a) shows the similar form with equation (1a), with $\eta(x - x_c)$ replacing $w(x)$. Thus equation (7a) can be seen as the equation of motion for a "virtual" beam structure spanning over Ξ, and equation (7b) can be seen as the boundary conditions, implying that the beam is simply supported at its two ends, *i.e.*, the boundaries of Ξ. Actually, Ξ can be arbitrarily selected along the span of the tested beam component, which is illustrated in Figure 1. And it can be seen from the figure that $q(x)$ in equation (7a) plays the role of external excitation applied on the axis of the "virtual" beam spanning over Ξ, with angular frequency of ω. Naturally, $\eta(x - x_c)$ in equation (7a) is regarded as the vibration deflection of the "virtual" beam. Reaching here, $\eta(x - x_c)$ can be calculated using classic mode superposition method, with a general form, as

$$\eta(x) = \sum_{r=1}^{\infty} \frac{Q_r}{\omega_r^2 - \omega^2} Y_r(x) \tag{8a}$$

where

$$Q_r = \int_0^{\tau} Y_r(x) q(x) \mathrm{d}x, \quad r = 1, 2 \ldots \tag{8b}$$

In the above equations, ω_r and $Y_r(x)$ are the rth natural angular frequency and mode shape of the "virtual" beam, and τ in equation (8b) corresponds to the length of the beam, equivalent as the length of Ξ. It is noteworthy that equations (8a) and (8b) are presented in general forms, and all the relevant functions are defined within $[0, \tau]$. In the following study, the first 100 modes of the "virtual" beam were superposed to construct the distribution of $\eta(x)$.

A variety of other forms of the damage index of VVD, different from the one shown in equation (5c), can be constructed by assuming boundary conditions different from equation (7b). For example, subject to a new type of boundary conditions as

$$\eta(\tau/2) = 0, \quad \eta(-\tau/2) = 0, \frac{\mathrm{d}\eta(\tau/2)}{\mathrm{d}x} = 0, \quad \frac{\mathrm{d}\eta(-\tau/2)}{\mathrm{d}x} = 0 \tag{9a}$$

the damage index of VVD exhibits a distinct form of

$$\begin{aligned} \overline{\mathrm{DI}}_{-VVD} = -EI\Bigg[& \frac{\mathrm{d}w(x_c + \tau/2)}{\mathrm{d}x} \cdot \frac{\mathrm{d}^2\eta(\tau/2)}{\mathrm{d}x^2} \\ & - \frac{\mathrm{d}w(x_c - \tau/2)}{\mathrm{d}x} \cdot \frac{\mathrm{d}^2\eta(-\tau/2)}{\mathrm{d}x^2} \Bigg] \\ & - EI\Bigg[w(x_c + \tau/2) \cdot \frac{\mathrm{d}^3\eta(\tau/2)}{\mathrm{d}x^3} \\ & - w(x_c - \tau/2) \cdot \frac{\mathrm{d}^3\eta(-\tau/2)}{\mathrm{d}x^3} \Bigg] \end{aligned} \tag{9b}$$

Equations (7a) and (9a) constitute the equation of motion of a "virtual" beam "clamped" at its two ends, instead of the simply supported one as shown in Figure 1. $\overline{\mathrm{DI}}_{-VVD}$ in equation (9b) can be constructed by measuring rotation angles and displacements of

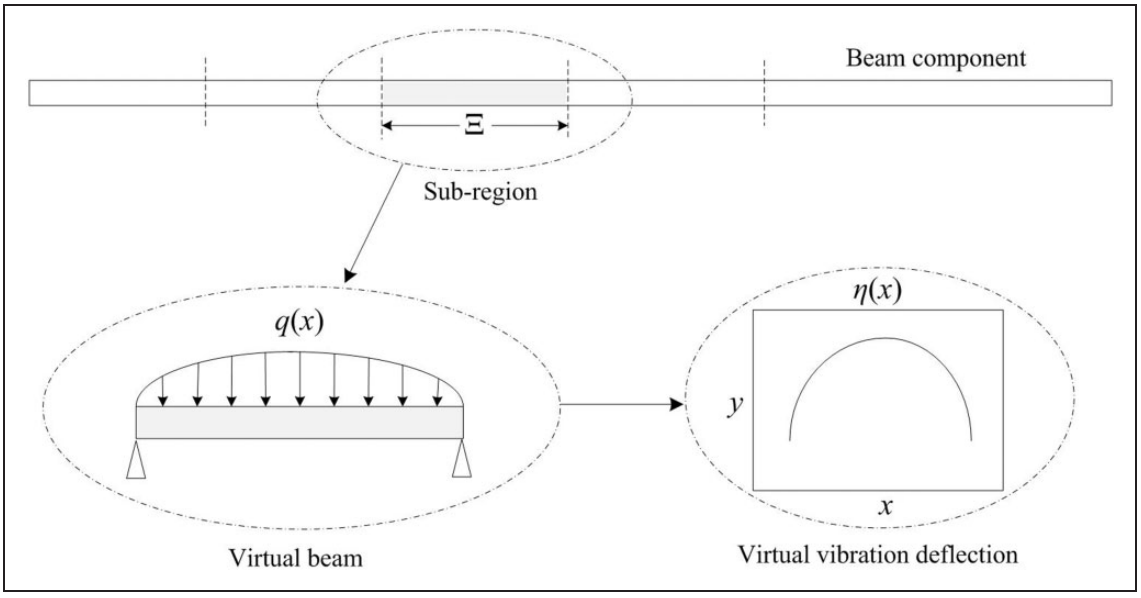

Figure 1. Schematic diagram illustrating the principle of virtual vibration deflection method.

vibration, and the distribution of $\eta(x)$ can be calculated following the same procedure as shown in equations (6a) to (6d), (8a) and (8b). It is certain that more forms of $\overline{\mathrm{DI}}_{-VVD}$ can be established by setting different types of boundary conditions. For simplicity, however, the form in equation (5c) was adopted in this study, relying on the measurements of vibration displacements and strains.

4. Numerical validation

When applying VVD, the entire structure under inspection was first divided into a series of sub-regions, equivalent as a series of Ξ, and the values of $\overline{\mathrm{DI}}_{-VVD}$ were then constructed according to equation (5c) within each sub-region, leading to an ultimate "region-by-region" detection signal distributed along the inspected structure. As a proof-of-concept investigation, the philosophy of VVD was examined using an FE model of a cantilever beam containing a small damaged zone.

4.1. Finite element model

Consider an Euler-Bernoulli cantilever beam with geometric and material properties listed in Table 1. The beam was clamped at its left end as shown in Figure 2. An FE model of the beam, with 1100 beam elements evenly distributing across the beam length, was created using commercial FEM code ANSYS®. A harmonic point excitation of 1000 Hz was applied at $x = 10$ mm (referring to Figure 2 for the coordinate system). A damaged zone spanning the region of [820 mm, 840 mm] was simulated by reducing Young's modulus of the modeled beam elements to 50% of the undamaged value. To avoid any singularity near the excitation, an inspection region of [200mm, 1100mm] was pre-determined to exclude the vicinity of the excitation point.

Table 1. Material and geometric properties of the simulated cantilever beam for numerical validation.

Properties	Numerical value
Density $\rho[\mathrm{kg/m^3}]$	2700
Young's Modulus E [GPa]	70
Beam length L[mm]	1100
Width b[mm]	10
Thickness h[mm]	10

The flexural displacement at each node (corresponding to the measurement point in the subsequent experiment) in the absence of noise interference, denoted by w_i^{exact}, was obtained using ANSYS®, which was then numerically contaminated with added noise as

$$w_i^{\mathrm{noisy}} = w_i^{\mathrm{exact}} \cdot (1 + \varepsilon_i) \cdot e^{j\varphi_i} \tag{10}$$

where w_i^{noisy} is the noise-corrupted counterpart of w_i^{exact}; ε_i a Gaussian random real number related to the magnitude of w_i^{exact} and φ_i another Gaussian random real number related to the phase of w_i^{exact}. In the succeeding analysis, $\mu(\varepsilon_i) = \mu(\varphi_i) = 0$, $\sigma(\varepsilon_i) = 1\%$ and $\sigma(\varphi_i) = 1^{\mathrm{o}}$($\mu$ and σ signify the mathematical manipulation of calculating mean and standard deviation, respectively). It should be emphasized that the level of noise interference is directly associated with $\sigma(\varepsilon_i)$ and $\sigma(\varphi_i)$, and can be expressed in a simple way. For example, $\sigma(\varepsilon_i) = 1\%$ and $\sigma(\varphi_i) = 1^{\mathrm{o}}$ was expressed as (1%, 1°). The distributions of w_i^{exact} and w_i^{noisy} with noise level of (1%, 1°) are plotted along the inspection region of the beam as shown in Figure 3.

4.2. Damage identification using the pseudo-excitation approach

Based on equation (1b), the damage index of the PE approach, without and with noise influence, was calculated using w_i^{exact} and w_i^{noisy}, respectively, leading to $\mathrm{DI}_i^{\mathrm{exact}}$ and $\mathrm{DI}_i^{\mathrm{noisy}}$ signals as presented in Figures 4(a) and (b), respectively. In Figure 4(a), the damaged zone

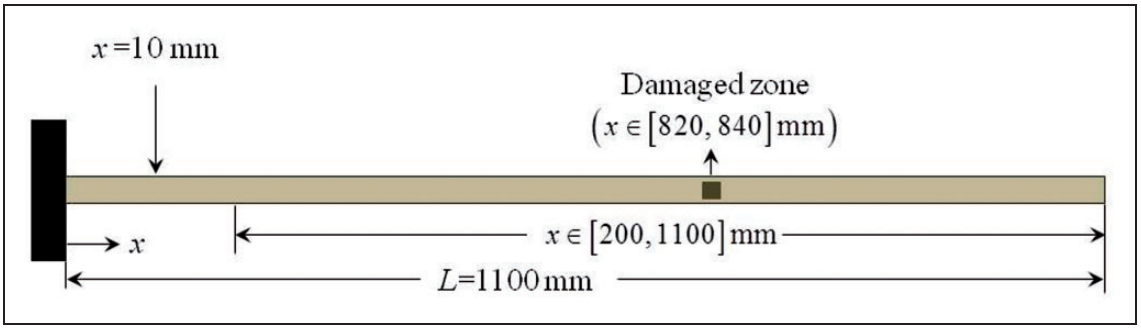

Figure 2. The finite element model of a cantilever beam bearing a small damaged zone.

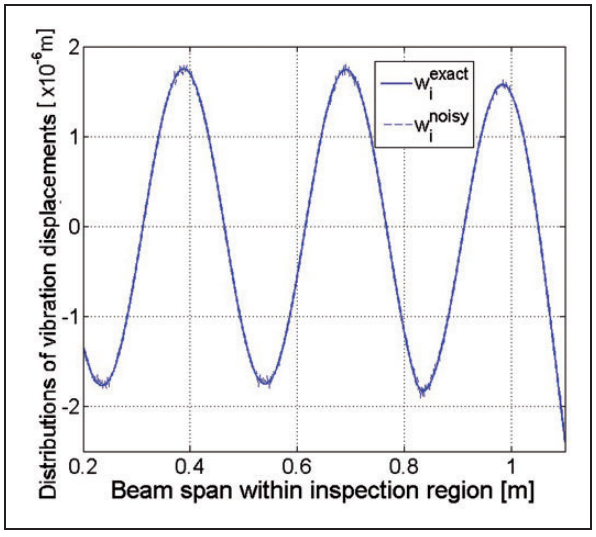

Figure 3. Distributions of w_i^{exact} and w_i^{noisy} along the inspection region of the cantilever beam in numerical validation, subject to vibration frequency of 1000 Hz.

can be exactly identified. On the contrary, the signal of $\text{DI}_i^{\text{noisy}}$ in Figure 4(b) fails to locate the damaged zone, as the added noise, though with a low level contained in vibration displacements (see Figure 3), was drastically magnified due to the fourth-order differentiation of $w(x)$ as shown in equations (1a) and (1b), and thus significantly masked the damage-induced feature as presented in Figure 4(a).

It was reported that the noise influence in the PE approach can be minimized by reducing the measurement density of vibration displacement to be around 10 measurement points per wavelength of vibration (Xu et al., 2011). And further reduction of measurement density brought an unacceptable truncation error in the relevant numerical computations, causing the loss of the accuracy of finite difference as shown in equation (1b). Thus, the measurement density in the current analysis was reduced to be 10 measurement points per wavelength, giving rise to $\text{DI}_i^{\text{exact}}$ and $\text{DI}_i^{\text{noisy}}$ signals as shown in Figure 4(c) and (d), respectively. In Figure 4(c), $\text{DI}_i^{\text{exact}}$ shows a single peak corresponding to the damaged zone, which is considered to be with decreased detection accuracy compared with Figure 4(a), from which two prominent peaks of the $\text{DI}_i^{\text{exact}}$ signal can be clearly observed at the boundaries of the damage, indicating both the location and the exact size of the damaged zone. On the other hand, significantly reduced noise influence is observed by comparing Figure 4(d) with (b). Under the noise influence, the detection accuracy was improved along with the reduction of measurement density, evidenced by the fact that the location of the damaged zone was indicated by one of the peaks of $\text{DI}_i^{\text{noisy}}$ signal in Figure 4(d). However, false peaks are observed at the intact regions of the beam, so the identification accuracy as presented in Figure 4(d) was still not satisfactory.

4.3. Damage identification using virtual vibration deflection

The values of $\kappa(x)$ involved in equation (5c), without any influence from measurement noise, can be calculated discretely using w_i^{exact} according to a central difference scheme, as

$$\kappa_i^{\text{exact}} = \frac{1}{\Delta^2}\left(w_{i-1}^{\text{exact}} - 2w_i^{\text{exact}} + w_{i+1}^{\text{exact}}\right) \tag{11a}$$

There are two ways of simulating κ_i values subject to noise influence from an experimental condition. One way relies on the derivation of w_i^{noisy} in equation (10), according to the central difference similar to equation (11a), as

$$\kappa_i^{\text{noisy-D}} = \frac{1}{\Delta^2}\left(w_{i-1}^{\text{noisy}} - 2w_i^{\text{noisy}} + w_{i+1}^{\text{noisy}}\right) \tag{11b}$$

where $\kappa_i^{\text{noisy-D}}$ indicates curvature derived from vibration displacement. The use of w_i^{noisy} and $\kappa_i^{\text{noisy-D}}$ typifies the application of an STVS-based VVD, because all terms in equation (5c) can be obtained based on the measurement of vibration displacements, *i.e.*, w_i^{noisy}. The noise influence in $\kappa_i^{\text{noisy-D}}$ comes from that in w_i^{noisy}, and was anticipated to be largely amplified due to the second-order derivation of w_i^{noisy}, as shown in equation (11b).

The other way of simulating a noise-contaminated κ_i is to directly introduce disturbance to κ_i^{exact} in equation (11a), as

$$\kappa_i^{\text{noisy-S}} = \kappa_i^{\text{exact}} \cdot (1 + \delta_i) \cdot e^{j\theta_i} \tag{11c}$$

where $\kappa_i^{\text{noisy-S}}$ simulates curvature from strain measurement (see equation (4)). In equation (11c), δ_i and θ_i are two Gaussian random real numbers related to the magnitude and phase of κ_i^{exact}, respectively. $\mu(\delta_i) = \mu(\theta_i) = 0$, and $\sigma(\delta_i)$ and $\sigma(\theta_i)$ signify the level of noise influence in $\kappa_i^{\text{noisy-S}}$, caused by errors in strain measurement. The use of w_i^{noisy} and $\kappa_i^{\text{noisy-S}}$ typifies the application of an MTVS-based VVD, since two types of vibration signatures, i.e., vibration displacement and strain, are involved in equation (5c).

The inspection region of the beam model was uniformly divided into 15 sub-regions, within which $\overline{\text{DI}}_{-VVD}$ were constructed according to equation (5c). The center position of each sub-region, i.e., x_c in equation (5c), is listed in Table 2, corresponding to the coordinate system shown in Figure 2. The curvature values in equation (5c) only need to be known at the

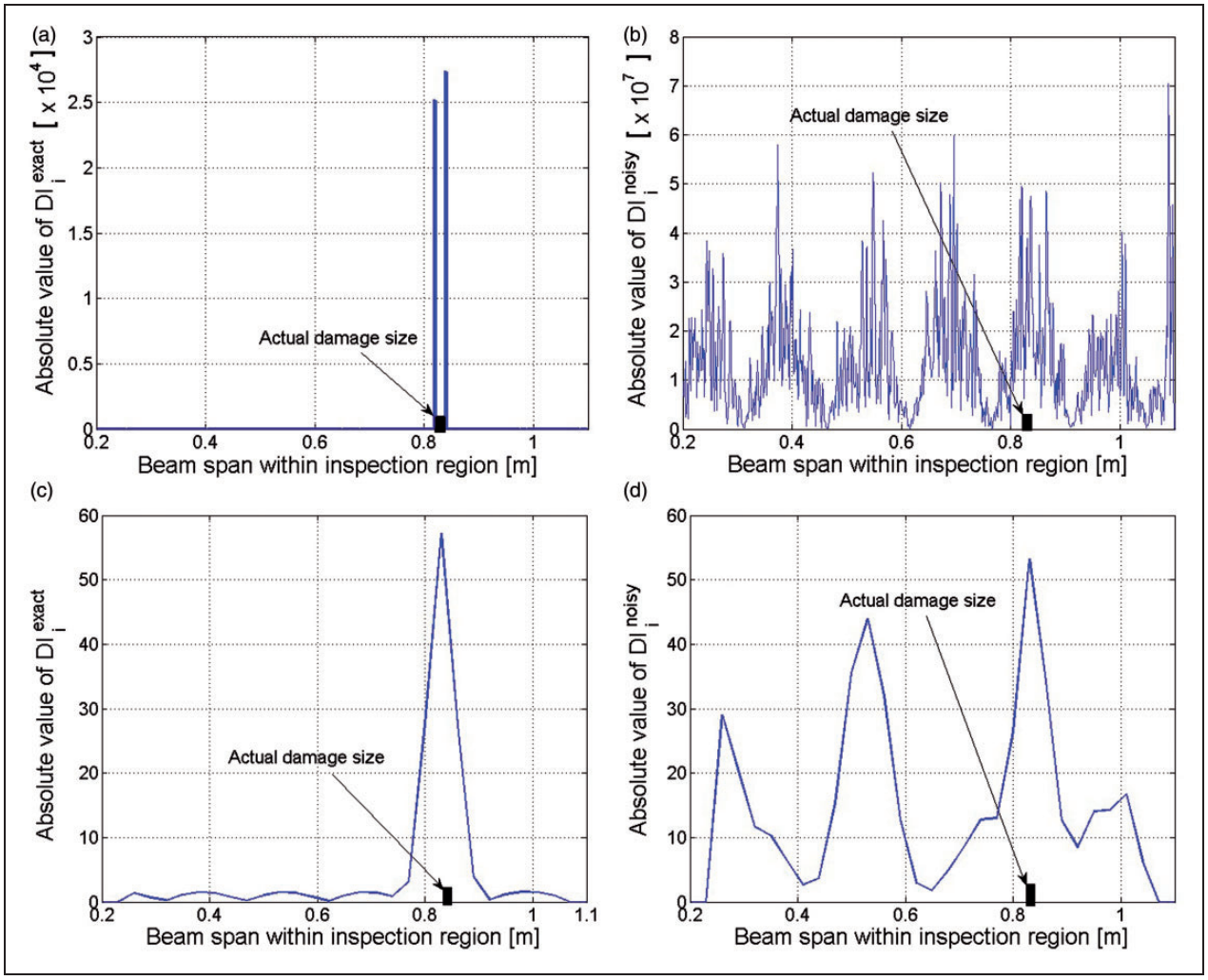

Figure 4. Constructed DI_i^{exact} and DI_i^{noisy} based on w_i^{exact} and w_i^{noisy}, respectively, corresponding to (a) and (b) 300 measurement points per wavelength of vibration, and (c) and (d) 10 measurement points per wavelength of vibration.

boundaries of the sub-regions, corresponding to 16 points evenly distributing along the inspection region. Within each sub-region, there are 61 points where vibration displacements, i.e., w_i^{exact} and w_i^{noisy}, were evenly captured. The vibration displacements were captured densely in order to construct the distribution of $q(x)$ according to equations (6b) to (6d) as accurately as possible. Figures 5(a) and (b) show the values of κ_i^{exact}, $\kappa_i^{noisy-D}$ and $\kappa_i^{noisy-S}$ at the boundaries of the sub-regions, calculated using equation (11a) to (11c), respectively. It can be seen in Figure 5(a) that the data of $\kappa_i^{noisy-D}$ was seriously disturbed data compared with κ_i^{exact}, because of the second-order derivation of w_i^{noisy} in equation (11b), as explained previously.Thus it is anticipated that the $\kappa_i^{noisy-D}$ signal may not be capable of providing reliable and accurate results for damage identification. In Figure 5(b), the noise level in $\kappa_i^{noisy-S}$ was set to be $\sigma(\delta_i) = 2\%$ and $\sigma(\theta_i) = 2^o$, *i.e.*, (2%, 2°)(referring to equation (11c)). A large similarity between $\kappa_i^{noisy-S}$ and κ_i^{exact} can be observed. A comprehensive comparison between Figures 5(a) and (b) implies that the MTVS-based VVD, constructed using w_i^{noisy} and $\kappa_i^{noisy-S}$, is capable of generating much superior accuracy of damage identification than that of the STVS-based VVD constructed using w_i^{noisy} and $\kappa_i^{noisy-D}$.

To implement VVD, first assign a specific form of the trial function, $\widetilde{q}(x)$, in equation (6c), as

$$\widetilde{q}(x) = \sin\left(\frac{\pi\left(x - x_c + \frac{\tau}{2}\right)}{\tau}\right), \quad x_c - \frac{\tau}{2} \le x \le x_c + \frac{\tau}{2} \tag{12}$$

Spanning over a sub-region, the profile of $\widetilde{q}(x)$ is similar with that of a half-period sine function. It is certain that $\widetilde{q}(x)$ can be assigned with other forms, and more suitable forms probably exist benefiting the effect of damage identification, but the relevant discussion is not included in the present study.

Based on $\widetilde{q}(x)$ in equation (12), $q(x)$ and $\eta(x)$ can be constructed accordingly using equations (6c), (6d), (8a) and (8b). In equation (6d), the value of c changes subject to different sub-regions due to the variation of $w(x)$ along the beam. Thus $q(x)$ and $\eta(x)$ also distribute differently in different sub-regions. c values corresponding to different sub-regions, calculated according to equation (6d) using w_i^{exact} and w_i^{noisy}, respectively, are listed in Table 2, and the variations of c subject to noise influence are also presented. It can be seen that the noise influence on c is minimal under the current noise level, *i.e.*, (1%, 1°) in w_i^{noisy}.

Table 2. Parameters associated with different sub-regions in numerical validation.

Center position x_c [m]	c based on w_i^{exact}	c based on w_i^{noisy}	Variation [%]
0.23	−0.6540	−0.6544	0.06
0.29	−0.6542	−0.6553	0.17
0.35	−0.6546	−0.6548	0.03
0.41	−0.6546	−0.6534	0.18
0.47	−0.6545	−0.6527	0.28
0.53	−0.6545	−0.6548	0.05
0.59	−0.6545	−0.6546	0.02
0.65	−0.6547	−0.6544	0.05
0.71	−0.6549	−0.6555	0.09
0.77	−0.6425	−0.6443	0.28
0.83	−0.6615	−0.6613	0.03
0.89	−0.6513	−0.6514	0.02
0.95	−0.6569	−0.6558	0.17
1.01	−0.6606	−0.6605	0.02
1.07	−0.6286	−0.6291	0.08

Figure 6(a) presents the $\overline{\text{DI}}_{-VVD}$ signal constructed based on equation (5c), using w_i^{noisy} and $\kappa_i^{\text{noisy-D}}$ as shown in equation (10) and (11b). The (STVS-based) $\overline{\text{DI}}_{-VVD}$ values are presented corresponding to the center positions of different sub-regions, *i.e.*, x_c in Table 2.

The sub-region containing the damaged zone is marked by a shadowed area. As anticipated, the STVS-based signal fails to reveal the damage location because of its vulnerability to noise influence. Subsequently, the MTVS-based $\overline{\text{DI}}_{-VVD}$ values were constructed using w_i^{noisy} and $\kappa_i^{\text{noisy-S}}$, with a noise level of (1%, 1°) in w_i^{noisy} and (2%, 2°) in $\kappa_i^{\text{noisy-S}}$. As shown in Figure 6(b), the signal shows satisfactory accuracy of identification, with strong noise immunity when compared with the noise-free $\overline{\text{DI}}_{-VVD}$ calculated based on w_i^{exact} and κ_i^{exact}. Therefore, it can be concluded according to Figures 6(a) and (b) that MTVS-based detection results possess much superior detection accuracy and noise immunity than those of STVS-based results. And the STVS-based VVD is not recommended to be used in an application, so the following parametric discussion is focused on the application of MTVS-based VVD exclusively.

4.4. Discussion

4.4.1. Noise immunity of multi-types of vibration signatures-based virtual vibration deflection. The level of noise

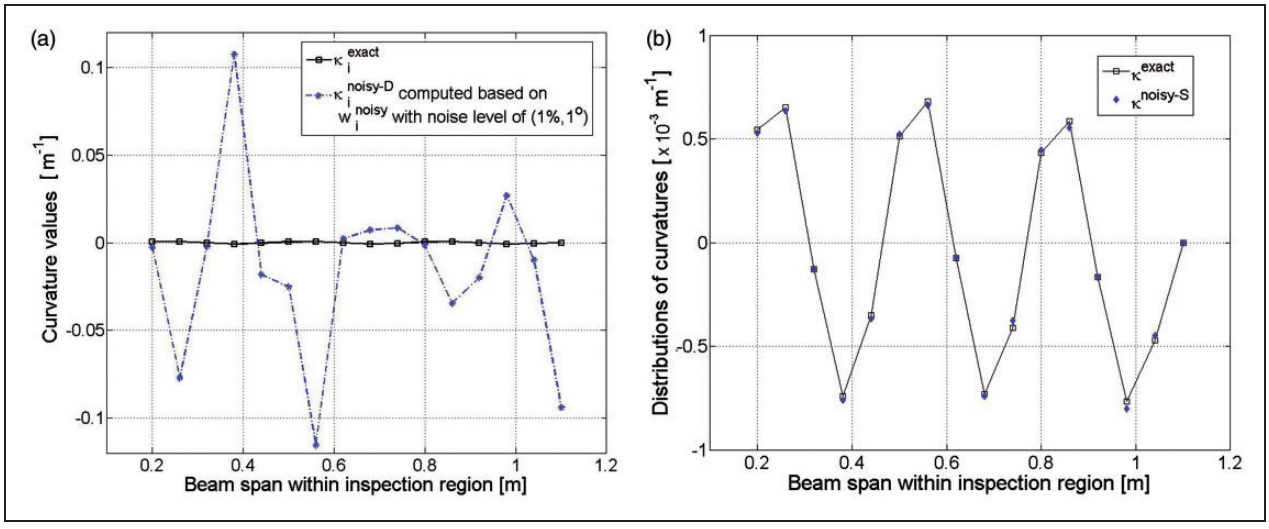

Figure 5. Distributions of curvature values at the boundaries of the sub-regions without noise influence as calculated using equation (11a) and with noise influence simulated relying on (a) the second-order derivation of w_i^{noisy} according to equation (11b) (with noise level of (1 %, 1°) in w_i^{noisy}), and (b) introduced disturbance according to equation (11c), with noise level of (2 %, 2°) added in κ_i^{exact}.

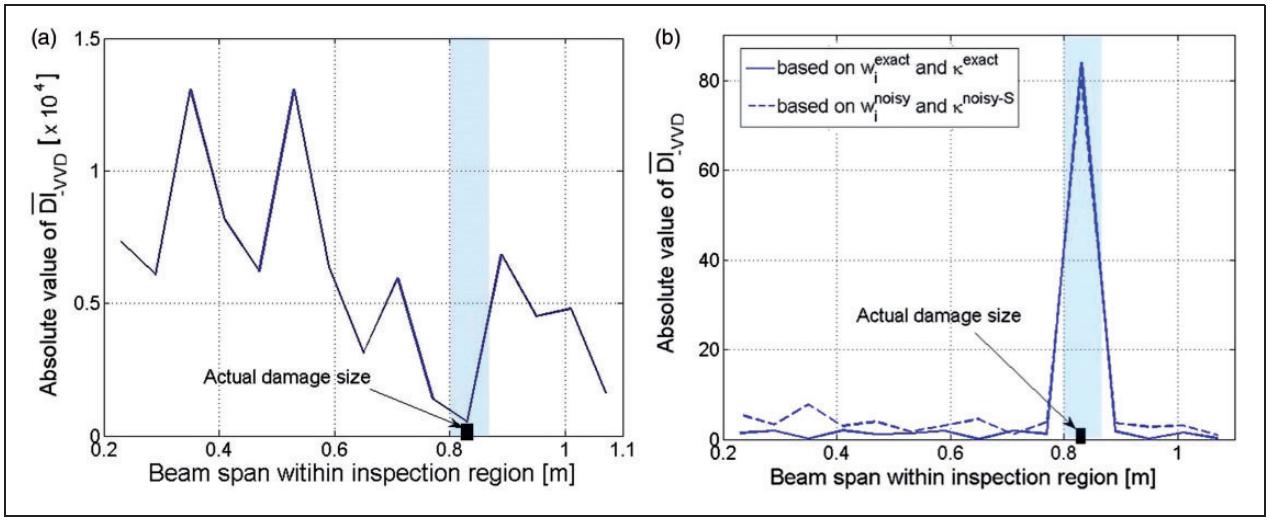

Figure 6. Distributions of the absolute values of (a) single-type of vibration signatures -based $\overline{DI}_{-VVD}$ constructed using w_i^{noisy} and $\kappa_i^{noisy-D}$and (b) noise-free $\overline{DI}_{-VVD}$ constructed using w_i^{exact} and κ_i^{exact}combined with multi-types of vibration signatures-based $\overline{DI}_{-VVD}$ constructed using w_i^{noisy} and $\kappa_i^{noisy-S}$, along the inspection region of the finite element model. The level of noise influence is (1%, 1°) in w_i^{noisy} and (2%, 2°) in $\kappa_i^{noisy-S}$.

influence contained in $\kappa_i^{noisy-S}$ was changed by adjusting the values of $\sigma(\delta_i)$ and $\sigma(\theta_i)$ in equation (11c), while the noise level in w_i^{noisy} was kept as (1%, 1°). The resultant signals of $\overline{DI}_{-VVD}$ are presented from Figures 7(a) to (f). It can be observed that satisfactory detection accuracy can be maintained under the noise level of (10%, 10°) in $\kappa_i^{noisy-S}$, referring to Figures 7(a) and (b). Increase of the noise level in $\kappa_i^{noisy-S}$ induces disturbances to the detection signals, as shown from Figure 7(c) to (e). But in these three figures, the signals can still facilitate to indicate the damage location, with their most prominent peak revealing the damage location, although false peaks are also seen at intact regions. Interestingly, it is discovered that a greater noise level does not necessarily lead to inferior detection accuracy and precision. For example, the indication of damage as presented in Figure 7(e), subject to noise level of (40%, 40°) in $\kappa_i^{noisy-S}$, seems even more accurate than those presented in Figure 7(c), subject to (20% , 20°) in $\kappa_i^{noisy-S}$, judging from less prominent fluctuations of $\overline{DI}_{-VVD}$ at intact regions in Figure 7(e). Such a phenomenon is attributed to the random nature of noise influence. In a statistical sense, however, detection results subject to lower noise level are still considered to be more precise and stable than that subject to severe noise interference. Further increased noise interference, with a level of (50%, 50°) in $\kappa_i^{noisy-S}$, led to the detection result shown in Figure 7(f), and it is clear that the damage can no longer be revealed under such a severe noise interference. In general, the MTVS-based VVD possesses considerably strong immunity to measurement noise in $\kappa_i^{noisy-S}$, capable of tolerating a noise level up to (10%, 10°). To obtain even higher noise tolerance, a large number of measurements can be carried out. By doing so, more detection signals can be constructed and then averaged, giving rise to a more stable result subject to less random disturbance.

Along the same way, influence from the measurement noise contained in w_i^{noisy} on the detection accuracy of MTVS-based VVD can be discussed, under a fixed noise level in $\kappa^{noisy-S}$. Two representative cases were presented in Figures 8(a) and (b), corresponding to noise levels of (5% , 5°) and (10%, 10°) in w_i^{noisy}, respectively. And the noise level in $\kappa^{noisy-S}$ was kept as (5%, 5°). According to the figures, a strong immunity of the MTVS-based VVD to noise interference in vibration displacements can be clearly seen.

4.4.2. Influence from measurement density of vibration displacements. It was anticipated that within an individual sub-region, changing the number of displacement measurement points, defined as N, will influence the detection accuracy of VVD evidently.

The reason is that in equation (6d), N directly determines the accuracy of the computation of c (e.g., larger N corresponds to smaller truncation error involved in the numerical integration in equation (6d)), thus will in turn determine the accuracy of the calculation of $q(x)$ in equation (6c), $\eta(x)$ in equation (8a), and $\overline{DI}_{-VVD}$ in equation (5c).

Figures 9(a) to (d) present the $\overline{DI}_{-VVD}$ signals subject to different values of N, under unchanged lengths of the sub-regions assigned previously and a fixed noise level of (1%, 1°) in w_i^{noisy} and (5%, 5°) in $\kappa^{noisy-S}$.

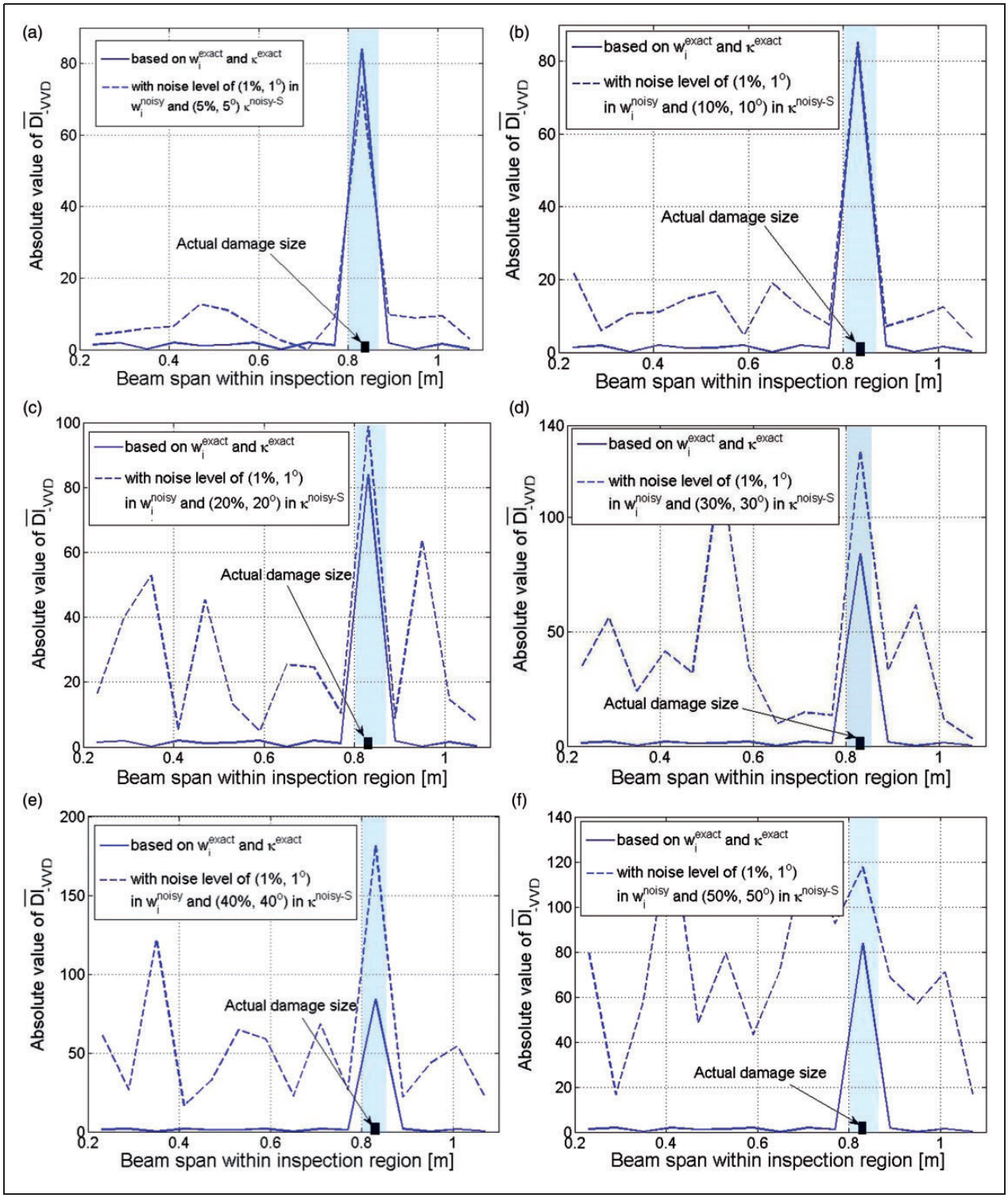

Figure 7. Distributions of the absolute values of the noise-free $\overline{DI}_{-VVD}$ constructed using w_i^{exact} and κ_i^{exact} and multi-types of vibration signatures-based $\overline{DI}_{-VVD}$ (using w_i^{noisy} and $\kappa_i^{noisy-S}$) subject to noise influence with the level of (1%, 1°) in w_i^{noisy} and (a) (5%, 5°), (b) (10%, 10°), (c) (20%, 20°), (d) (30%, 30°), (e) (40%, 40°), and (f) (50%, 50°) in $\kappa_i^{noisy-S}$.

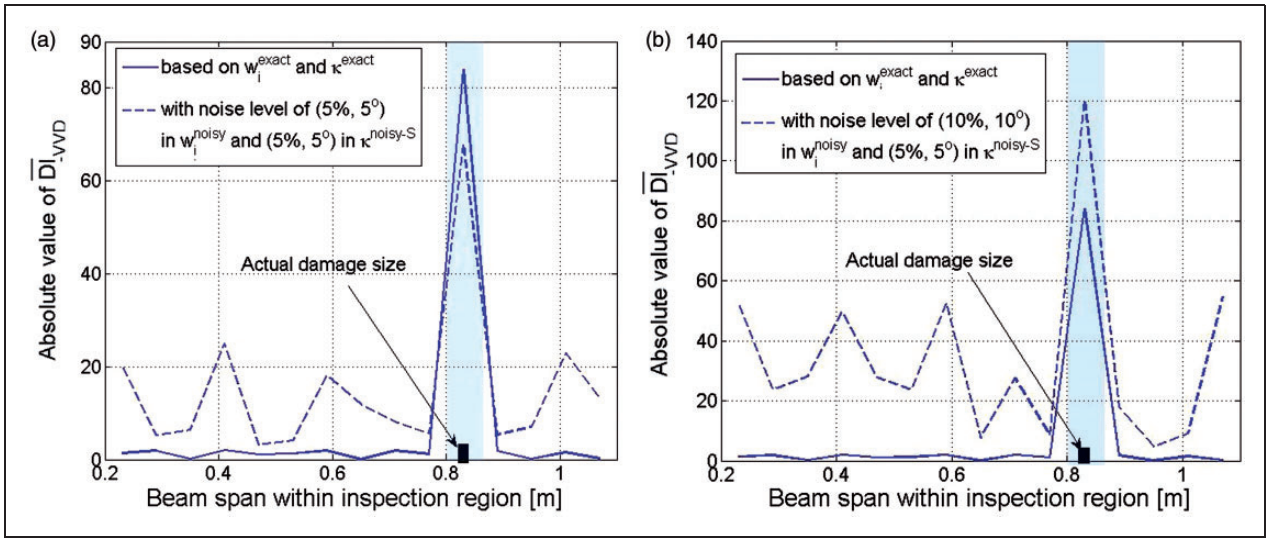

Figure 8. Distributions of the absolute values of the noise-free $\overline{DI}_{-VVD}$ constructed using w_i^{exact} and κ_i^{exact} and multi-types of vibration signatures-based $\overline{DI}_{-VVD}$ (using w_i^{noisy} and $\kappa_i^{noisy-S}$) subject to noise influence with the level of (5%, 5°) in $\kappa_i^{noisy-S}$ and (a) (5%, 5°) and (b) (10%, 10°) in w_i^{noisy}.

Progressively decreasing accuracy along with reduced N values were observed, as shown from Figures 9(a) to (d). The capability of damage indication was maintained until $N = 16$ (in Figure 9(c)), and a sharp decrease of detection accuracy was encountered when N was reduced from 16 to 13. As shown in Figure 9(d), the $\overline{DI}_{-VVD}$ signal corresponding to $N = 13$ is not capable of locating damage.

It is important that from Figures 9(a) to (d), the observation and analysis of the noise-free signals of $\overline{DI}_{-VVD}$, constructed based on w_i^{exact} and κ_i^{exact}, play a major role. Because compared with signals showing great instability due to the random influence from noise, noise-free signals reflect the variations of the accuracies of relevant numerical computations (e.g., numerical computation of equation (6d)) more accurately, in turn providing a more solid reference for selecting N. In addition, the distribution of a noise-influenced signal was constructed based on a noise-free one. If a noise-free signal fails to locate damage, so does its noisy counterpart. Therefore, according to the noise-free signals of $\overline{DI}_{-VVD}$ as shown in Figure 9(a) to (d), $N > 15$ was concluded as the basic requirement when applying VVD. It can be seen that to achieve satisfactory detection accuracy based on VVD, a large number of displacement measurement points is usually needed to be assigned along the tested structure, which may cause inconvenience for practical measurement under certain circumstances. Thus further study is necessary to be developed aimed at reducing the influence from N on the detection accuracy.

5. Experimental validation

5.1. Setup

Experimental validation was subsequently conducted to further scrutinize the detection accuracy of VVD, in identifying multiple defects in a cantilever beam-like structure, as sketched in Figure 10(a). The structure was made of aluminum 6061 with a density of 2700 kg/m^3 and a Young's modulus of 68.9 GPa. The defined inspection region, shown in Figure 10(a), features a length of 550 mm, a constant width of 30 mm and a uniform thickness of 8 mm, within which two through-width notches (1.2 mm × 30 mm × 2 mm), each accounting for 0.2% of the entire beam span, were created at 220 mm and 380 mm from the clamped end, as shown in Figure 10(b). Notably, the irregular shape of the structure, referring to the varying width near the free end, was intentionally designed in order to demonstrate the effectiveness of VVD in detecting damage in structural components with complex boundary geometries. A harmonic excitation of 1000 Hz was applied with an electromechanical shaker (B&K®4809), near the free end of the structure. A scanning Doppler laser vibrometer (Polytec®PSV- 400B) was used to measure the flexural vibration displacements at 283 measurement points (with a spacing interval around 2 mm), along the central line of the beam.

Within the inspection region, thirteen impedance strain gauges (manufactured by Huangyan Testing Apparatus Factory, Zhejiang, China; the product type of the strain gauges is BX120-3AA and the serial

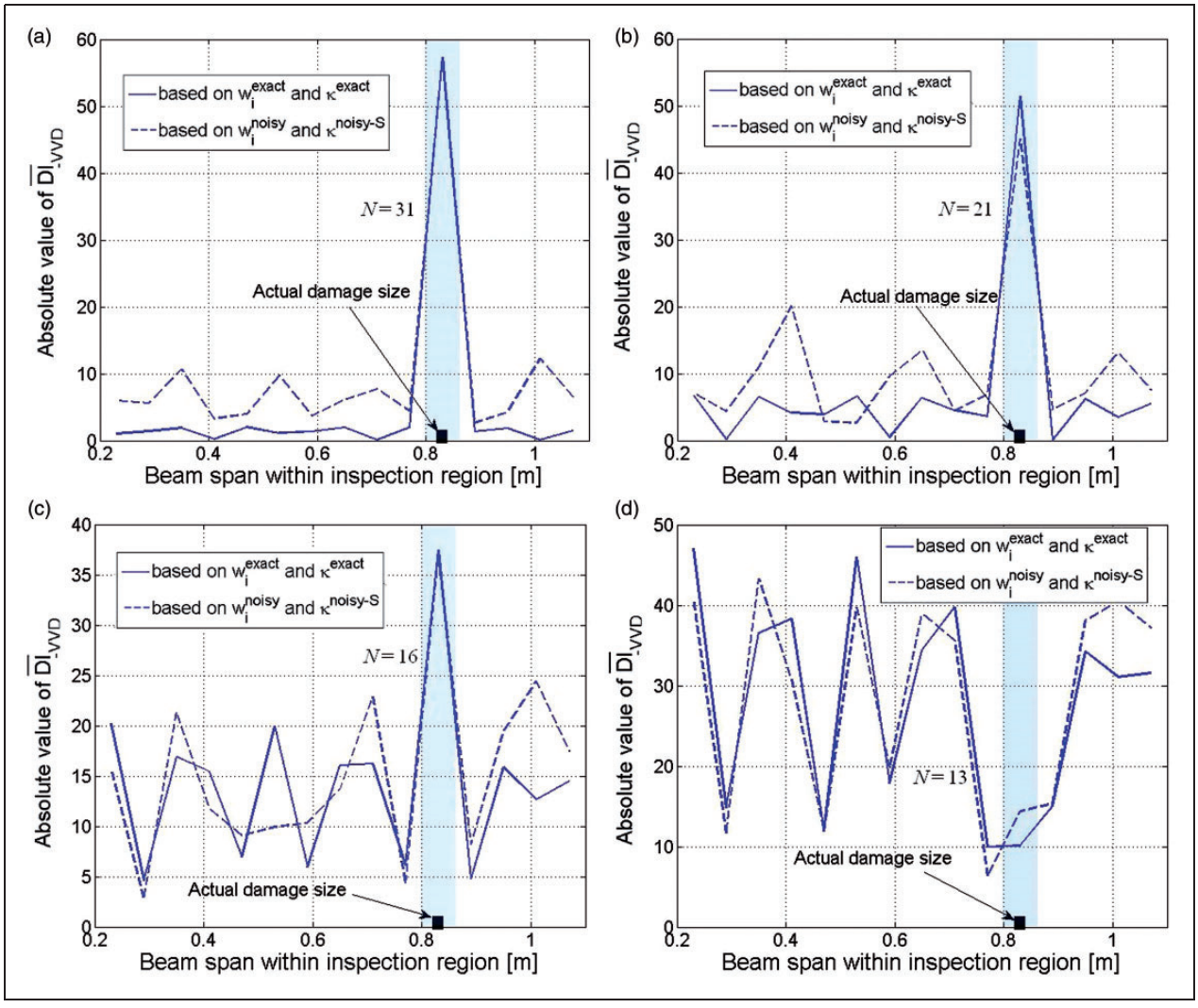

Figure 9. Distributions of the absolute values of the noise-free $\overline{DI}_{-VVD}$ (using w_i^{exact} and κ_i^{exact}) and multi-types of vibration signatures-based $\overline{DI}_{-VVD}$ (using w_i^{noisy} and $\kappa_i^{noisy-S}$) subject to (a) 31, (b) 21, (c) 16, and (d) 13 measurement points of vibration displacements within each sub-region. The level of noise influence in the noisy $\overline{DI}_{-VVD}$ signal is (1%, 1°) in w_i^{noisy} and (5%, 5°) in $\kappa_i^{noisy-S}$.

number is 105) were attached on the surface of the structure with uniform adjacent distances. Thus 12 sub-regions were formed, within which the notches were identified. The length of each sub-region is 40 mm, and the center positions, x_c, of different sub-regions are listed in Table 3, referring to the coordinate system as shown in Figure 10(a). The data of dynamic strains were captured using a universal recorder (Kyowa®EDX-100A) and the curvature values were then calculated according to equation (4). Between adjacent strain gauges, there are around 20 measurement points of vibration displacements, i.e., $N \approx 20$.

5.2. Results

The PE approach was firstly applied according to equation (1b), and the detection signal constructed using all measurement points of vibration displacements is shown in Figure 11(a).

As predicted in Section 4.2, the signal is drastically disturbed and the damage-related information has been totally masked. By adjusting the measurement density to be 10 measurement points per wavelength, improved detection accuracy was achieved as shown in Figure 11(b). It can be seen that the notch corresponding to $x = 380$ mm can be identified, but the other notch cannot be clearly revealed because of the serious fluctuations of the detection signal at intact regions.

The STVS- and MTVS-based detection signals of VVD are presented in Figure 12(a) and (b), respectively. In Figure 12(a), the notch corresponding to $x = 220$mm seems to be identified by the STVS-based signal, whereas the other one corresponding to $x = 380$mm cannot be revealed. However, the signal

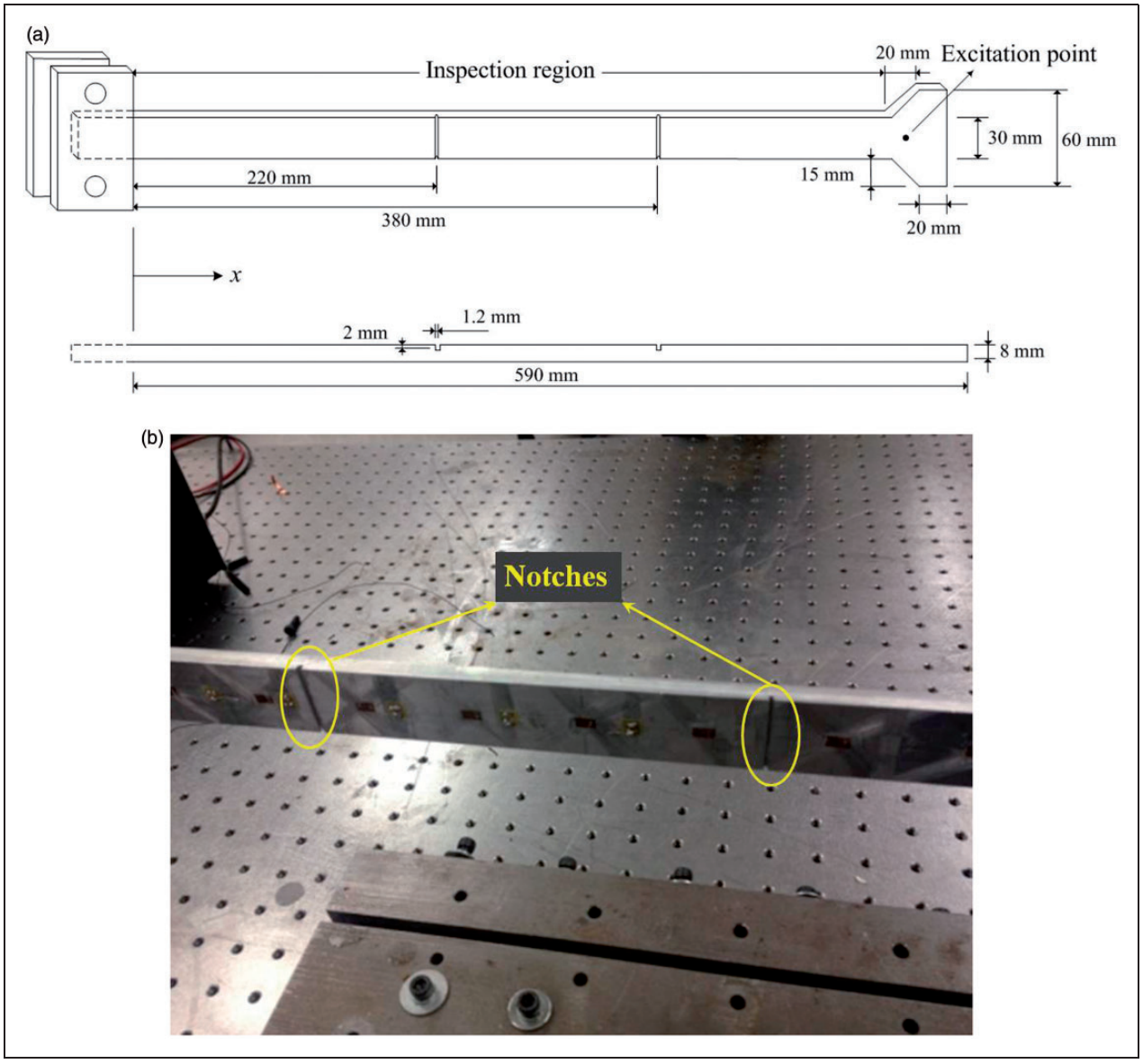

Figure 10. (a) Schematic of a cantilever beam-like structure bearing two notches and (b) the photo of the notches and strain gauges (six strain gauges are visible along the centerline of the specimen).

Table 3. Center positions (x_c) of different sub-regions in experimental validation.

x_c [m]	0.06	0.10	0.14	0.18	0.22	0.26	0.30	0.34	0.38	0.42	0.46	0.50

is not considered to be reliable because of the severe noise influence included in the curvature values, referring to Figures 6(a) and 5(a). Thus the indication of one of the notches, although successful, was doubted as a coincidence arising from the random distribution of measurement noise. In Figure 12(b), the locations of both notches were accurately identified by the MTVS-based VVD signal, featured by two prominent peaks of $\overline{\mathrm{DI}}_{-VVD}$ corresponding to the sub-regions containing the notches.

Higher detection precision of VVD is expected to be achieved by increasing the number of sub-regions along the inspected structure, using a larger number of strain gauges. And the accuracy of identification can be further increased by arranging a larger number of measurement points of vibration displacements between

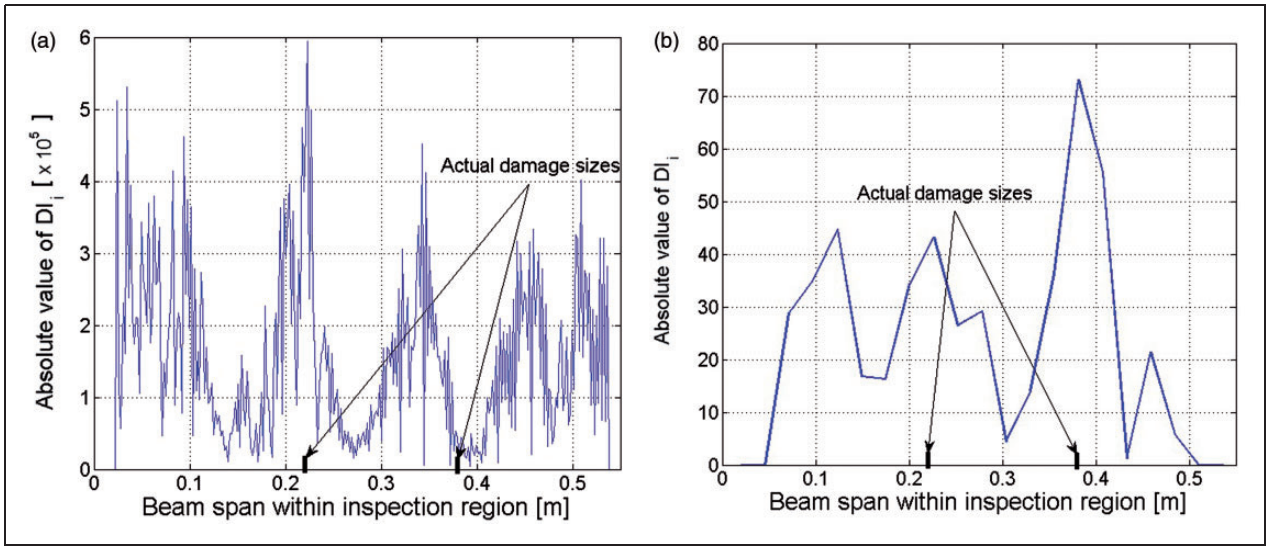

Figure 11. Distributions of the experimental damage identification results constructed based on the pseudo-excitation approach using (a) 150 measurement points per wavelength of vibration, and (b) 10 measurement points per wavelength of vibration.

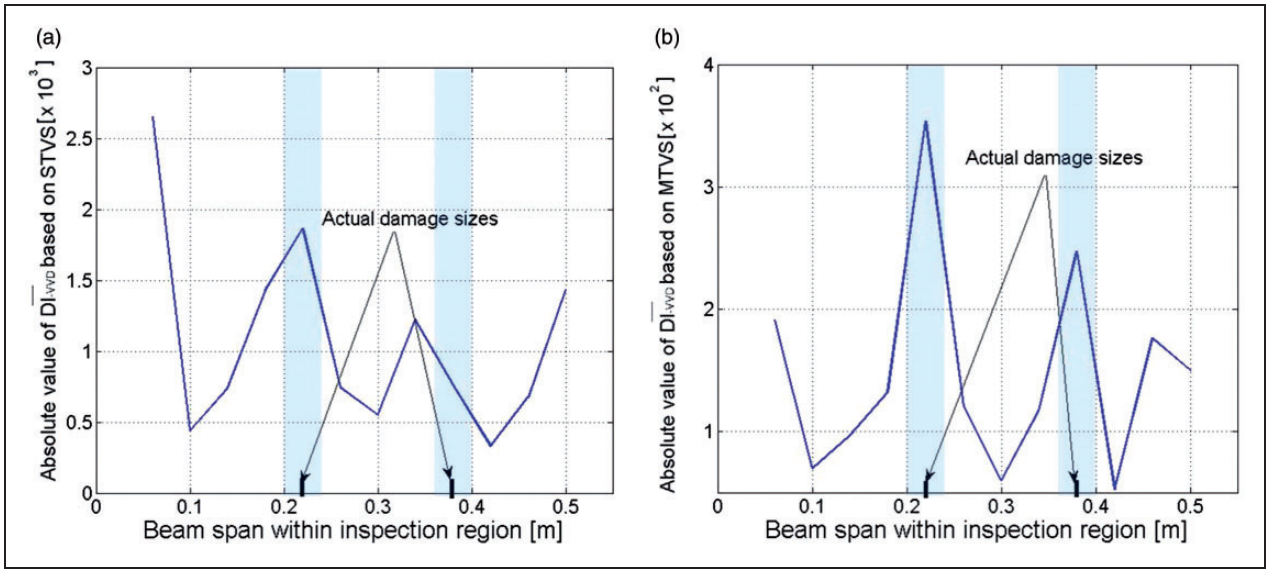

Figure 12. Distributions of the experimental damage identification results constructed based on virtual vibration deflection using measured (a) vibration displacements (single-type of vibration signatures) and (b) vibration displacements combined with dynamic strains (multi-types of vibration signatures).

adjacent strain gauges, as evidenced by Figures 9(a) to (d). In fact, the level of noise influence associated with the current experiment was considered to be relatively severe, probably because of the interference from a variety of attachments to the surface of the specimen (such as wires connected to the strain gauges) on the linearity of the vibration of the specimen. Thus, it is anticipated that identification accuracy can be improved by making use of advanced and compact experimental configurations, for instance, using new types of strain sensors (e.g., Fiber Bragg Grating sensor) or more reasonable wire arrangements.

6. Conclusion

Virtual vibration deflection was established based on the "weak" formulation of the PE approach. By dividing the entire structure under inspection into a series of sub-regions, each sub-region was regarded as a "virtual" structure undergoing independent vibration

subject to different types of boundary conditions, which can be assigned arbitrarily. The vibration deflection of the ''virtual'' structure, calculated according to classic mode superposition method, is equivalent as the weighting function in the ''weak'' formulation of the PE, and can be used to construct the damage index of VVD.

The application of VVD is free of baseline signals, benchmark structures, prior-knowledge of structural boundary conditions, etc. And compared with the PE, VVD possesses improved detection accuracy, attributed to a hybrid use of MTVS in its formulation. Relying on numerical analysis, VVD shows a high tolerance of measurement noise both contained in vibration displacements and strains. Within an individual subregion of identification, the number of measurement points for vibration displacements larger than 15 was considered as a basic requirement for applying VVD. Finally, in experimental validation, the detection results demonstrated the effectiveness of VVD in identifying through width notches in beam-like structures. Lastly, it should be noticed that because of the interference from measurement noise, fluctuations of detection results of VVD cannot be totally eliminated at the intact regions of inspected structures, inducing difficulty in declaring the successful identification of damage. Thus, a more comprehensive algorithm is necessary to be developed, obtaining a threshold associated with the level of noise influence and the correlation between the damage index and the severity of damage, according to which damage can be identified with higher confidence.

Funding

This work was supported by the National Natural Science Foundation of China (grant numbers 51375414 and 11272272). This work was also supported by the Hong Kong Research Grants Council via General Research Fund (GRF) (grant numbers 15214414 and 523313).

References

Abdo MAB and Hori M (2002) A numerical study of structural damage detection using changes in the rotation of mode shapes. *Journal of Sound and Vibration* 251: 227–239.

Aoki Y and Byon OI (2001) Damage detection of CFRP pipes and shells by using localized flexibility method. *Advanced Composite Materials* 10: 189–198.

Cao MS, Ostachowicz W, Bai RB, et al. (2013a) Fractal mechanism for characterizing singularity of mode shape for damage detection. *Applied Physics Letters* 103: 221906.

Cao MS, Ostachowicz W, Radzienski M, et al. (2013b) Multiscale shear-strain gradient for detecting delamination in composite laminates. *Applied Physics Letters* 103: 101910.

Chen J, Su Z and Cheng L (2010) Identification of corrosion damage in submerged structures using fundamental anti-symmetric Lamb waves. *Smart Material & Structures* 19(1): 015004.

Ciambella J and Vestroni F (2015) The use of modal curvature for damage localization in beam-type structures. *Journal of Sound and Vibration* 340: 126–137.

Fan W and Qiao P (2011) Vibration-based damage identification methods: a review and comparative study. *Structural Health Monitoring: An International Journal* 10: 83–29.

Farrar CR, Nix DA, Scott W, et al. (2001) Vibration-based structural damage identification. *Philosophical Transactions: Mathematical, Physical and Engineering Sciences* 359: 131–149.

Giurgiutiu V (2005) Tuned lamb wave excitation and detection with piezoelectric wafer active sensors for structural health monitoring. *Journal of Intelligent Material Systems and Structures* 16(4): 291–305.

Guo HY and Li ZL (2011) A two-stage method for damage detection using frequency responses and statistical theory. *Journal of Vibration and Control* 18(2): 191–200.

He L, Lian J and Ma B (2014) Intelligent damage identification method for large structures based on strain modal parameters. *Journal of Vibration and Control* 20(12): 1783–1795.

Ihn JB and Chang FK (2008) Pitch-catch active sensing methods in structural health monitoring for aircraft structures. *Structural Health Monitoring: An International Journal* 7: 5–19.

Kawiecki G (2001) Modal damping measurement for damage detection. *Smart Materials and Structures* 10: 466–471.

Kim JT, Ryu YS, Cho HM, et al. (2003) Damage identification in beam-type structures: frequency-based method vs. mode-shape-based method. *Engineering Structures* 25: 57–67.

Lee YS and Chung MJ (2000) A Study on crack detection using eigen-frequency test data. *Computers and Structures* 77: 327–342.

Liu TY, Chiang WL, Chen CW, et al. (2011) Identification and monitoring of bridge health from ambient vibration data. *Journal of Vibration and Control* 17(4): 589–603.

Montalvao D, Maia NMM and Ribeiro AMR (2006) A review of vibration-based structural health monitoring with special emphasis on composite materials. *The Shock and Vibration Digest* 38(4): 295–324.

Pandey AK, Biswas M and Samman MM (1991) Damage detection from changes in curvature mode shapes. *Journal of Sound and Vibration* 145(2): 321–332.

Pau A, Greco A and Vestroni F (2010) Numerical and experimental detection of concentrated damage in a parabolic arch by measured frequency variations. *Journal of Vibration and Control* 17(4): 605–614.

Qiao P, Lu K, Lestari W, et al. (2007) Curvature mode shape-based damage detection in composite laminated plates. *Composite Structures* 80(2): 409–428.

Sohn H, Lim HJ, DeSimio MP, et al. (2014) Nonlinear ultrasonic wave modulation for online fatigue crack detection. *Journal of Sound and Vibration* 333(5): 1473–1484.

Stubbs N and Kim JT (1996) Damage localization in structures without baseline modal parameters. *AIAA Journal* 34(8): 1644–1649.

Su Z, Yang C, Pan N, Ye L and Zhou LM (2007) Assessment of delamination in composite beams using shear horizontal (SH) wave mode. *Composites Science and Technology* 67(2): 244–251.

Su Z, Cheng L, Wang X, Yu L and Zhou C (2009) Predicting delamination of composite laminates using an imaging approach. *Smart Materials and Structures* 18(7): 074002.

Tomaszewska A (2010) Influence of statistical errors on damage detection based on structural flexibility and mode shape curvature. *Computers and Structures* 88: 154–164.

Wang X, Hu N, Fukunaga H, et al. (2001) Structural damage identification using static test data and changes in frequencies. *Engineering Structures* 23: 610–621.

Wang XM, Foliente G, Su Z and Ye L (2006) Multilevel decision fusion in a distributed active sensor network for structural damage detection. *Structural Health Monitoring– An International Journal* 5(1): 45–58.

Xu H, Cheng L, Su ZQ, et al. (2011) Identification of damage in structural components based on locally perturbed dynamic equilibrium. *Journal of Sound and Vibration* 330: 5963–5981.

Xu H, Cheng L, Su ZQ, et al. (2013a) Damage visualization based on local dynamic perturbation: theory and application to characterization of multi-damage in a plane structure. *Journal of Sound and Vibration* 332: 3438–3462.

Xu H, Cheng L, Su ZQ, et al. (2013b) Reconstructing interfacial force distribution for identification of multi-debonding in steel-reinforced concrete structure using noncontact laser vibrometry. *Structural Health Monitoring* 12: 507–521.

Xu H, Su ZQ, Cheng L, et al. (2015) A ''pseudo-excitation'' approach for structural damage identification: from ''strong'' to ''weak'' modality. *Journal of Sound and Vibration* 337: 181–198.

Xu W, Radzieński M, Ostachowicz W and Cao MS (2013c) Damage detection in plates using two-dimensional directional Gaussian wavelets and laser scanned operating deflection shapes. *Structural Health Monitoring: An International Journal* 12(5-6): 457–468.

Yan AM and Golinval JC (2005) Structural damage localization by combining flexibility and stiffness methods. *Engineering Structures* 27: 1752–1761.

Zhang XH, Zhu S, Xu YL, et al. (2011) Integrated optimal placement of displacement transducers and strain gauges for better estimation of structural response. *International Journal of Structural Stability and Dynamics* 11(3): 581: 602.

Zhao X, Gao H, Zhang G, et al. (2007) Active health monitoring of an aircraft wing with embedded piezoelectric sensor/actuator network: I. defect detection, localization and growth monitoring. *Smart Materials and Structures* 16: 1208–1217.

Zhou C, Su Z and Cheng L (2011) Probability-based diagnostic imaging using hybrid features extracted from ultrasonic Lamb wave signals. *Smart Materials and Structures* 20(12): 125005.